

PERMANENTS OF MATRIX ENSEMBLES: COMPUTATION, DISTRIBUTION, AND GEOMETRY

IGOR RIVIN

ABSTRACT. We report on a computational and experimental study of permanents. On the computational side, we use the GPU to greatly accelerate the computation of permanents over \mathbb{C} , \mathbb{R} , \mathbb{F}_p and \mathbb{Q} . In particular, we use this to compute the permanents of DFT and Schur matrices far beyond the ranges hitherto known. On the experimental side, we present two new observations. First, for Haar-distributed unitary matrices U , the permanent $\text{perm}(U)$ follows a circularly-symmetric complex Gaussian distribution $\mathcal{CN}(0, \sigma^2)$ — we confirm this via a number of tests for n up to 23 with 50,000 samples. The DFT matrix permanent is an extreme outlier for every prime $n \geq 7$. In contrast, for Haar-random *orthogonal* matrices O , the permanent $\text{perm}(O)$ is approximately real Gaussian but with positive excess kurtosis that decays as $O(1/n)$, indicating slower convergence. For matrices with Gaussian entries (GUE, GOE, Ginibre), the permanent follows an α -stable distribution with stability index $\alpha \approx 1.0\text{--}1.4$, well below the Gaussian value $\alpha = 2$.

Secondly, we study the permanent along geodesics on the unitary group. For the geodesic from the identity to the n -cycle permutation matrix, we find a universal scaling function $f(t) = \frac{1}{n} \ln |\text{perm}(\gamma(t))|$ that is independent of n in the large- n limit, with a midpoint value

$$\text{perm}(\gamma(\frac{1}{2})) = (-1)^{(n-1)/2} \cdot 2e^{-n} \left(1 + \frac{1}{3n} + O(n^{-2})\right)$$

for odd n and zero for even n . For the geodesic to the DFT matrix, the permanent recovers 10–40 times above its valley minimum when n is prime, but not when n is composite — a geodesic fingerprint of primality.

1. INTRODUCTION

The permanent of an $n \times n$ matrix $A = (a_{ij})$,

$$\text{perm}(A) = \sum_{\sigma \in S_n} \prod_{i=1}^n a_{i, \sigma(i)},$$

is one of the most studied and least tractable objects in algebraic combinatorics. Unlike the determinant, no polynomial-time algorithm is known (or expected) for computing the permanent of a general matrix; the problem

Date: February 12, 2026.

2020 Mathematics Subject Classification. 15A15, 81P68 (primary); 60B20, 11C20, 05A15 (secondary).

Key words and phrases. permanent, boson sampling, anti-concentration, quantum information, GOE, GUE.

is $\#P$ -complete even over $\{0, 1\}$ [15]. The fastest known general algorithm, due to Ryser [11], runs in $O(n 2^n)$ time.

Despite this worst-case complexity, the permanent admits rich structure in special families. A particularly natural family consists of the *unitary* matrices $U \in U(n)$. Here the permanent has gained prominence through *boson sampling*: Aaronson and Arkhipov [1] showed that the output probabilities of an n -photon linear optical network are given by $|\text{perm}(U_S)|^2$, where U_S is an $n \times n$ submatrix of the network's unitary transfer matrix. Their hardness proof—and with it, a leading proposal for demonstrating quantum computational advantage—hinges on the assumption that permanents of Haar-random unitaries anti-concentrate, formalized as the Permanent Anti-Concentration Conjecture (PACC) [1, 4]. Experimental implementations using photonic circuits [16, 3] have now reached regimes where classical simulation of the output distribution is computationally challenging.

The *Schur matrix* $S_n = (e^{2\pi i j k / n})_{j,k=0}^{n-1}$, whose normalized version S_n / \sqrt{n} is the discrete Fourier transform, plays a distinguished role: its permanent defines the integer sequence OEIS A003112, and its magnitude as a function of n remains poorly understood. The DFT also features in *suppression laws* for multi-photon interference: Tichy [12] showed that certain submatrix permanents of the DFT vanish, governing which transition amplitudes are suppressed in Fourier multi-port interferometers.

In this paper we report three sets of results.

- (1) **Computation.** We develop a pipeline combining the Chinese Remainder Theorem (CRT) with Gray-code-parallelized Ryser evaluation on GPU, achieving a 200–400× speedup over single-threaded CPU. This lets us extend the known values of $\text{perm}(S_n)$ from $n = 35$ to $n = 43$.
- (2) **Distribution.** We sample permanents of Haar-distributed random unitary matrices and find that $\text{perm}(U)$ follows a circularly-symmetric complex Gaussian distribution. The DFT matrix is an extreme outlier for prime n . For orthogonal matrices, $\text{perm}(O)$ is approximately real Gaussian but with excess kurtosis that decays as $O(1/n)$. In contrast, for matrices drawn from Gaussian ensembles (GUE, GOE, Ginibre), the permanent follows an α -stable distribution with $\alpha \approx 1.0\text{--}1.4$, indicating heavy tails and infinite variance.
- (3) **Geodesics.** We study how the permanent evolves along geodesics on $U(n)$. The geodesic from I to the n -cycle permutation matrix yields a universal scaling function with a clean midpoint asymptotic. The geodesic to the DFT matrix distinguishes primes from composites.

2. COMPUTATIONAL METHODS

2.1. CRT-based exact computation. The Schur matrix S_n has entries ω^{jk} where $\omega = e^{2\pi i / n}$. When $p \equiv 1 \pmod{n}$, the group $(\mathbb{Z}/p\mathbb{Z})^\times$ contains a primitive n th root of unity g , and we may compute $\text{perm}(S_n) \pmod{p}$ by evaluating the permanent of the integer matrix $(g^{jk} \pmod{p})$ using Ryser's

algorithm over $\mathbb{Z}/p\mathbb{Z}$. Combining sufficiently many such primes via the Chinese Remainder Theorem recovers the exact integer $\text{perm}(S_n)$.

The number of primes needed is determined by the bound $|\text{perm}(S_n)| \leq n^{n/2}$, which follows from the classical inequality $|\text{perm}(U)| \leq 1$ for unitary U [7] applied to the normalized DFT matrix S_n/\sqrt{n} . For $n = 43$ this requires 12 primes, each needing an independent Ryser evaluation over $2^{43} \approx 8.8 \times 10^{12}$ subsets.

2.2. Gray code block parallelization. Following [6], we parallelize Ryser's formula by partitioning the 2^n subsets into contiguous Gray code blocks, one per thread. Each thread initializes its block's starting row-sum vector in $O(n)$ time, then iterates through the block with $O(1)$ work per subset (a single column addition or subtraction, followed by a product accumulation). This achieves near-linear parallel scaling and is the key to effective GPU utilization.

2.3. GPU acceleration. We implement the Gray-code-block Ryser kernel in CUDA, distributing $\sim 10^6$ blocks across the streaming multiprocessors of an NVIDIA H100 GPU. All arithmetic is performed in 64-bit integers. The GPU achieves $11\text{--}13\times$ speedup over a 64-core CPU for the mod- p kernel, and $20\text{--}30\times$ for a specialized mod-3 kernel using the bipedal \mathbb{F}_2 encoding of [6]. Our computations of the exact integer values of the Schur permanent 4, 2, 23, 88, and 424 minutes for $n = 37, 39, 41, 43$ respectively, consistent with the expected $\sim 4\times$ scaling per increment of 2 in n .

3. DISTRIBUTION OF $|\text{perm}(U)|$ FOR HAAR UNITARIES

3.1. Experimental setup. For each odd prime $n \in \{7, 11, 13, 17, 19, 23\}$, we generate 50,000 independent Haar-distributed unitary matrices $U \in U(n)$ (via QR decomposition of complex Gaussian matrices with diagonal phase correction [8]) and compute $\text{perm}(U)$ using a GPU-batched Ryser kernel (one CUDA thread per matrix).

3.2. Complex Gaussian distribution.

Observation 1. *For Haar-distributed $U \in U(n)$ with $n \geq 5$, the permanent $\text{perm}(U)$ is well-described by a circularly-symmetric complex Gaussian $\mathcal{CN}(0, \sigma^2)$; equivalently, $|\text{perm}(U)|$ follows a Rayleigh distribution with parameter $\sigma(n)$.*

Recall that if $Z \sim \mathcal{CN}(0, \sigma^2)$, then $|Z|$ has the Rayleigh distribution with scale $\sigma/\sqrt{2}$, so the magnitude and complex distributional statements are equivalent. Moreover, since $|Z|^2 = \text{Re}(Z)^2 + \text{Im}(Z)^2$ is the sum of two independent $N(0, \sigma^2/2)$ squares, the *squared amplitude* is exponentially distributed:

$$(1) \quad |\text{perm}(U)|^2 \sim \text{Exp}(\text{mean } \sigma^2), \quad \Pr[|\text{perm}(U)|^2 \geq x] = e^{-x/\sigma^2},$$

with $\sigma^2 = n!/n^n$. This is the complex analog of the Porter–Thomas distribution [9]—the universal squared-amplitude statistics for eigenstates of random Hamiltonians in quantum chaos. In the boson sampling context (Section 7.3), the output probabilities of a Haar-random linear optical network are proportional to $|\text{perm}(U_S)|^2$, so an exponential law for the squared permanent directly governs the statistics of photon detection events.

We test the complex Gaussian hypothesis in two complementary ways.

Magnitude (Rayleigh). Figure 1 presents Q–Q plots of $|\text{perm}(U)|$ against the fitted Rayleigh distribution for $n = 7, 11, 13, 17, 19, 23$ (50,000 samples each). The agreement is excellent: Kolmogorov–Smirnov p -values range from 0.23 to 0.92, and Weibull shape parameters satisfy $c \in [1.98, 2.03]$ (the Rayleigh distribution is the special case $c = 2$).

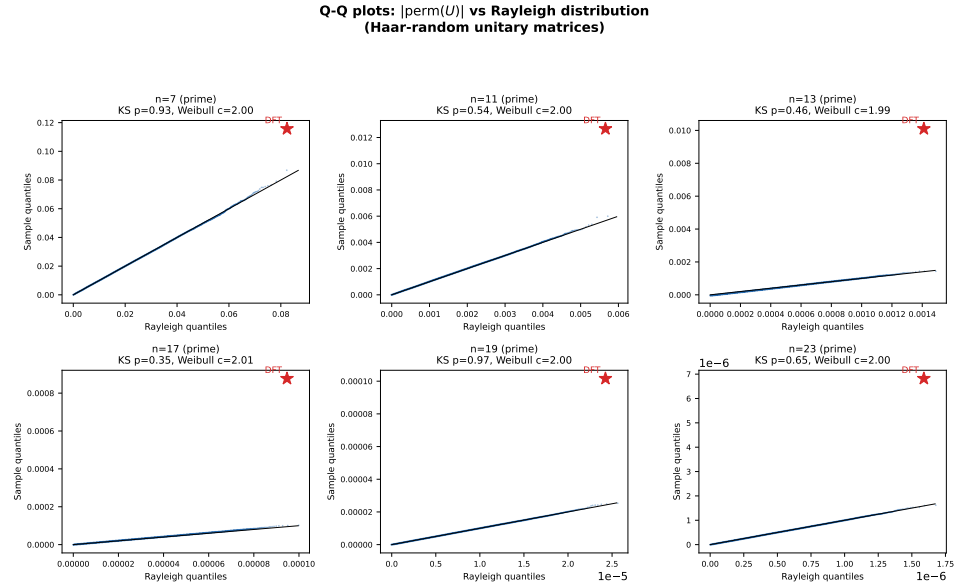


FIGURE 1. Q–Q plots of $|\text{perm}(U)|$ against the Rayleigh distribution for Haar-random unitary matrices, $n = 7, 11, 13, 17, 19, 23$ (50,000 samples each). The red star marks the DFT matrix, which lies beyond the 100th percentile for every n shown. Weibull shape parameters c and KS p -values are shown in each panel title.

Complex structure. Figure 2 tests the full complex Gaussian hypothesis via three diagnostics. The scatter plots of $(\text{Re perm}(U), \text{Im perm}(U))$ are circularly symmetric, with variance ratio $\sigma_R/\sigma_I \in [0.97, 1.01]$ and Pearson correlation $|r| < 0.01$. The Mahalanobis distances d_k^2 follow χ_2^2 (Q–Q plots in the middle row), confirming bivariate normality via Mardia’s skewness test ($p > 0.03$ for all n , with most $p > 0.1$). The phase $\arg(\text{perm}(U))$ is

uniform on $[0, 2\pi)$ (bottom row; KS $p > 0.23$ for all n). Finally, circularity ($\mathbb{E}[Z^2] = 0$) is confirmed by a bootstrap test of the pseudocovariance, with $|\hat{p}|/\hat{\sigma}^2 < 0.01$ in all cases.

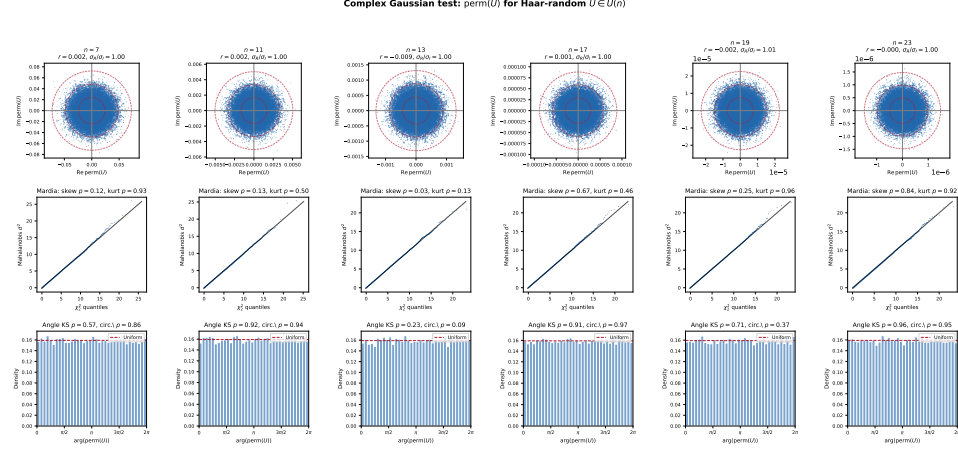


FIGURE 2. Complex Gaussian tests for $\text{perm}(U)$ with Haar-random $U \in U(n)$, $n = 7, 11, 13, 17, 19, 23$ (50,000 samples each). Top: scatter plots of (Re, Im) with 1σ – 3σ circles. Middle: Q–Q plots of Mahalanobis d^2 against χ^2 . Bottom: phase histograms against the uniform density.

The fitted variance $\hat{\sigma}^2(n) \approx n!/n^n \sim \sqrt{2\pi n} e^{-n}$ matches the exact second moment $\mathbb{E}[|\text{perm}(U)|^2] = n!/n^n$ computed via Weingarten calculus [10] to within a few percent. The exponential factor e^{-n} governs the “typical size” of a Haar-random permanent; equivalently, $|\text{perm}(U)| \sim e^{-n/2}$ with high probability.

A heuristic justification: the permanent is a sum of $n!$ complex terms $\prod_i U_{i,\sigma(i)}$, each of magnitude $\sim n^{-n/2}$. For large n , by a central-limit-type argument, this sum approaches a complex Gaussian, whose magnitude is Rayleigh. Making this rigorous would require establishing sufficient decorrelation among the summands, which we leave as an open problem.

Remark 2. While the complex Gaussian form is broadly consistent with the Porter-Thomas heuristic from quantum chaos (output amplitudes of random quantum processes are complex Gaussian) and with the CLT intuition that the permanent—a sum of $n!$ weakly correlated terms—should be approximately Gaussian, we are not aware of any prior work that explicitly identifies or tests this distributional form for $\text{perm}(U)$. The anti-concentration literature (e.g. [10, 4]) studies moments and tail bounds but does not identify the full distribution.

3.3. DFT outlier for prime n .

Observation 3. For every odd prime n with $7 \leq n \leq 29$, the DFT permanent $|\text{perm}(S_n/\sqrt{n})|$ exceeds all 50,000 Haar-random samples, placing it at the 100th percentile. For composite odd n (such as $n = 9$ or $n = 15$), the DFT permanent falls within the bulk of the distribution.

This dichotomy is summarized in Table 1.

TABLE 1. DFT percentile and ratio to maximum sampled value.

n	Type	DFT percentile	$ \text{perm}(F_n) /\max_{\text{sample}}$
7	prime	100%	1.6×
9	composite	34%	—
11	prime	100%	2.5×
13	prime	100%	6.9×
15	composite	14%	—
17	prime	100%	10.0×
19	prime	100%	16.0×
23	prime	100%	38.1×

The ratio $|\text{perm}(F_n)|/\max_{\text{sample}}$ grows rapidly with n for primes, indicating that the DFT is not merely in the tail but *far beyond* the natural range of the Rayleigh distribution.

4. PERMANENTS ALONG GEODESICS ON $U(n)$

The unitary group $U(n)$ carries a natural bi-invariant Riemannian metric. Given a unitary matrix U with Schur decomposition $U = Q \text{diag}(e^{i\theta_1}, \dots, e^{i\theta_n}) Q^*$, the geodesic from I to U is

$$\gamma(t) = Q \text{diag}(e^{it\theta_1}, \dots, e^{it\theta_n}) Q^*, \quad t \in [0, 1].$$

We study $|\text{perm}(\gamma(t))|$ as a function of t for two natural choices of endpoint.

4.1. Geodesic to the n -cycle. Let C_n be the cyclic permutation matrix $(C_n)_{ij} = \delta_{i,j+1 \bmod n}$. Its eigenvalues are $\omega^k = e^{2\pi i k/n}$ for $k = 0, \dots, n-1$, and it is diagonalized by the DFT matrix. The geodesic $\gamma(t)$ is therefore a circulant matrix with explicit entries

$$(2) \quad \gamma(t)_{jl} = \frac{e^{2\pi i t} - 1}{n(e^{2\pi i (l-j+t)/n} - 1)},$$

having magnitude $\sin(\pi t)/(n |\sin(\pi(l-j+t)/n)|)$.

Observation 4 (Universal scaling). Define

$$f(t) = -\frac{1}{n} \ln |\text{perm}(\gamma(t))|$$

. Then $f(t)$ converges to a universal function of t as $n \rightarrow \infty$, with the properties:

- (i) *Symmetry*: $f(t) = f(1-t)$.
- (ii) *Boundary*: $f(0) = f(1) = 0$.
- (iii) *Minimum*: $f(\frac{1}{2}) = 1$ (i.e. $|\text{perm}(\gamma(\frac{1}{2}))| \sim e^{-n}$).
- (iv) *Gaussian onset*: $f(t) \approx \frac{\pi^2}{3}t^2$ for $t \ll 1$.

Figure 3 (left panel) shows the collapse of $f(t)$ across $n = 5, 7, \dots, 23$. The convergence to a single curve is evident.

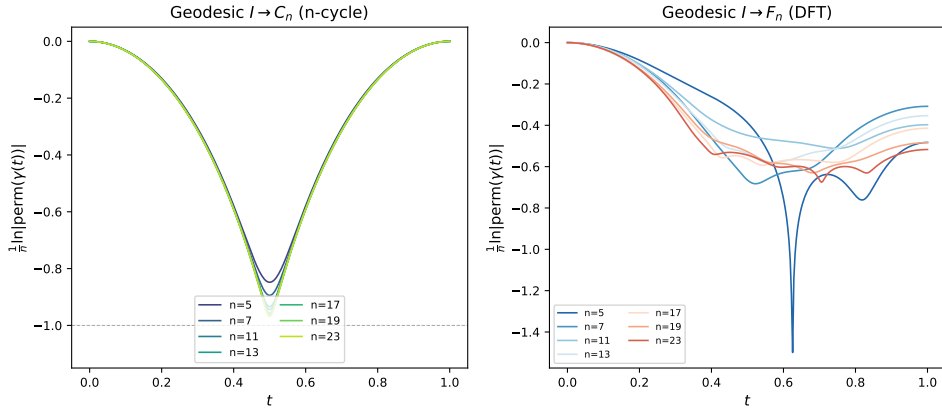


FIGURE 3. Scaled permanent $\frac{1}{n} \ln |\text{perm}(\gamma(t))|$ along geodesics on $U(n)$. Left: geodesic $I \rightarrow C_n$ showing universal collapse; the dashed line marks -1 . Right: geodesic $I \rightarrow F_n$ (DFT) for various primes.

Observation 5 (Midpoint asymptotic). *For the midpoint $\gamma(\frac{1}{2})$ of the geodesic $I \rightarrow C_n$:*

- (i) *If n is odd*: $\text{perm}(\gamma(\frac{1}{2})) = (-1)^{(n-1)/2} \cdot 2e^{-n} (1 + \frac{1}{3n} + O(n^{-2}))$.
- (ii) *If n is even*: $\text{perm}(\gamma(\frac{1}{2})) = 0$.

Table 2 presents the numerical evidence. The ratio $|\text{perm}(\gamma(\frac{1}{2}))|/(2e^{-n})$ converges to 1 with correction term $1/(3n)$ verified to four-digit accuracy.

Remark 6 (Phase cancellation). The permanent of the entry-wise absolute value matrix $|\gamma(\frac{1}{2})|$ grows as $\sim 1.32^n$, while the actual permanent decays as $\sim e^{-n}$. The complex phases therefore cancel all but a fraction $e^{-n}/1.32^n \approx (0.28)^n$ of the magnitude — roughly n decades of cancellation for moderate n .

Remark 7 (Real-valuedness). The permanent $\text{perm}(\gamma(t))$ is real for all $t \in [0, 1]$ (numerically, $|\text{Im perm}|/|\text{Re perm}| < 10^{-14}$). This follows from the circulant symmetry: $\gamma(t)$ is a circulant with first row related by complex conjugation to its last row (reversed), so the Ryser sum is invariant under complex conjugation.

TABLE 2. Midpoint permanent of the n -cycle geodesic.

n	$\text{perm}(\gamma(\frac{1}{2}))$	$ \text{perm} /(2e^{-n})$	$n \cdot (\text{perm} /(2e^{-n}) - 1)$
5	$+1.440 \times 10^{-2}$	1.0686	0.343
7	-1.912×10^{-3}	1.0486	0.340
11	-3.443×10^{-5}	1.0307	0.338
13	$+4.638 \times 10^{-6}$	1.0260	0.337
17	$+8.444 \times 10^{-8}$	1.0198	0.336
19	-1.140×10^{-8}	1.0177	0.336
23	-2.082×10^{-10}	1.0146	0.335

4.2. Geodesic to the DFT matrix. The normalized DFT matrix $F_n = S_n/\sqrt{n}$ is unitary. The geodesic $I \rightarrow F_n$ also passes through a valley, but unlike the cycle case, the behavior at $t = 1$ depends strongly on the arithmetic of n .

Observation 8 (Prime vs. composite recovery). *Let*

$$r(n) = |\text{perm}(F_n)| / \min_{t \in [0,1]} |\text{perm}(\gamma(t))|$$

and measure how much the DFT permanent recovers above the geodesic valley. Then:

- For odd prime n : $r(n) \in [14, 161]$ (recovery of 1–2 decades).
- For composite n ($n = 9, 15$): $r(n) \in [1.1, 2.7]$ (negligible recovery).

This provides a “geodesic fingerprint” of primality: the number-theoretic structure of the DFT organizes the permanent upward precisely when n is prime.

4.3. Complex trajectories. Figure 4 shows the complex trajectory $\text{perm}(\gamma(t))$ for both geodesics. For the cycle geodesic (bottom row), the permanent remains real-valued, decaying symmetrically from $\text{perm} = 1$ at $t = 0, 1$ to the midpoint minimum, with the sign pattern $(-1)^{(n-1)/2}$ visible as the alternation of + and – regions across different n . For the DFT geodesic (top row), the trajectory sweeps out an increasingly circular arc in the complex plane: starting at $\text{perm} = 1$, the permanent acquires a large imaginary part before returning to a tiny real value at $t = 1$. The near-circularity of this arc for large n is striking and unexplained.

5. ORTHOGONAL MATRICES: A REAL COUNTERPART

We repeat the distributional analysis for the orthogonal group. Since $O \in O(n)$ is real, $\text{perm}(O)$ is a *real* random variable. If the complex Gaussian for unitaries arose purely from a CLT mechanism, we would expect $\text{perm}(O) \sim N(0, \sigma^2)$ for Haar-random O .

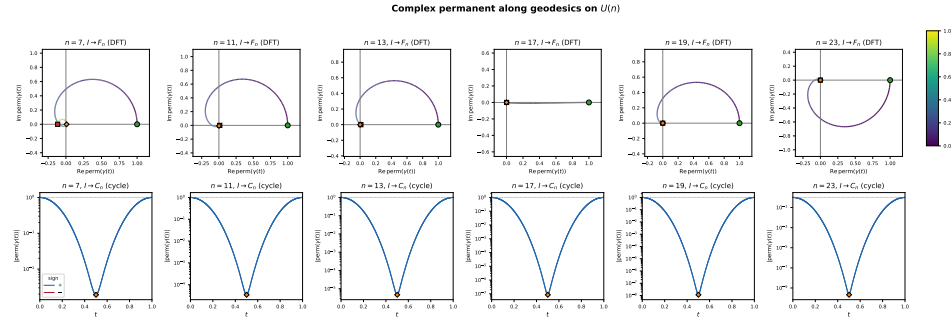


FIGURE 4. Complex trajectory of $\text{perm}(\gamma(t))$ along geodesics on $U(n)$ for $n = 7, 11, 13, 17, 19, 23$. Top: DFT geodesic $I \rightarrow F_n$, colored by t ; green circle marks $t = 0$, red square marks $t = 1$, orange diamond marks $t = 1/2$. Bottom: cycle geodesic $I \rightarrow C_n$ (log scale); the permanent is real-valued, with blue/red indicating sign.

5.1. Approximate normality with excess kurtosis. For each $n \in \{7, 11, 13, 17, 19, 23\}$, we generate 50,000 Haar-random orthogonal matrices and compute $\text{perm}(O)$ using the same GPU pipeline. The distribution is symmetric and bell-shaped (Figure 5), but normality tests reveal systematic *excess kurtosis* that decreases with n :

TABLE 3. Excess kurtosis of $\text{perm}(O)$ for Haar-random $O \in O(n)$.

n	$\text{Var}[\text{perm}(O)]$	Excess kurtosis	SW p -value
7	7.89×10^{-4}	0.607	$< 10^{-4}$
11	3.88×10^{-6}	0.418	$< 10^{-4}$
13	2.60×10^{-7}	0.212	0.001
17	1.14×10^{-9}	0.145	0.12
19	7.61×10^{-11}	0.083	0.19

Observation 9. For Haar-distributed $O \in O(n)$, the permanent $\text{perm}(O)$ is approximately Gaussian with mean zero, but with positive excess kurtosis that decreases as $O(1/n)$. The convergence to Gaussian is markedly slower than in the unitary case, where all normality tests pass already at $n = 7$.

The positive excess kurtosis (leptokurtosis) means heavier tails than Gaussian — the orthogonal permanent produces occasional large values more often than a Gaussian would predict. This is consistent with the heuristic that the orthogonal group has $n(n-1)/2$ degrees of freedom (versus n^2 for the unitary group), so the CLT-like cancellation among the $n!$ Ryser terms proceeds more slowly.

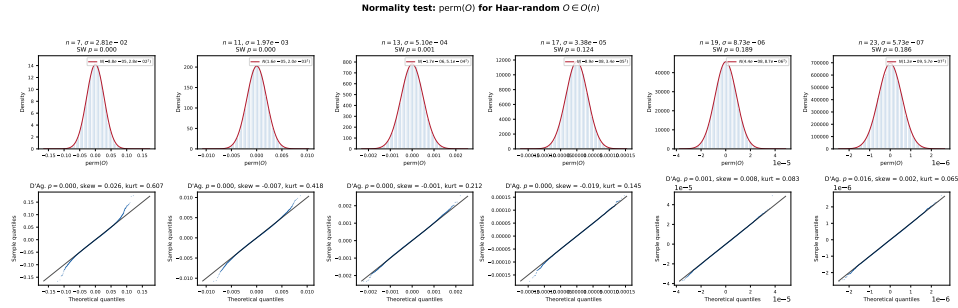


FIGURE 5. Normality test for $\text{perm}(O)$ with Haar-random $O \in O(n)$ (50,000 samples each). Top: histograms with fitted normal density. Bottom: Q–Q plots. Excess kurtosis is visible in the heavy tails for small n but diminishes with increasing n .

5.2. Variance scaling. The variance $\sigma^2(n) = \text{Var}[\text{perm}(O)]$ decays exponentially, but significantly *faster* than the unitary second moment $n!/n^n \sim \sqrt{2\pi n} e^{-n}$ (Figure 6). The ratio $\text{Var}[\text{perm}(O)]/(n!/n^n)$ decreases from 0.13 at $n = 7$ to 0.001 at $n = 19$. This discrepancy arises because the orthogonal Weingarten function differs from its unitary counterpart: the real entries of $O \in O(n)$ have stronger correlations (with $n(n-1)/2$ rather than n^2 degrees of freedom), which amplifies the cancellation in the Ryser sum and reduces the variance.

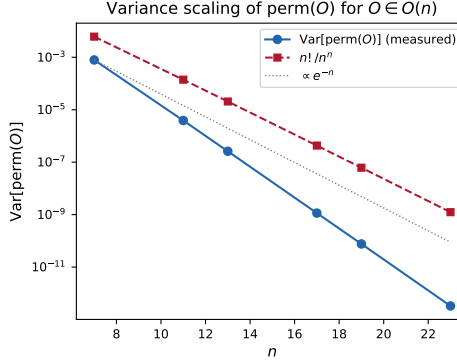


FIGURE 6. Variance of $\text{perm}(O)$ for Haar-random $O \in O(n)$, compared with the unitary second moment $n!/n^n$. The orthogonal variance decays faster.

Remark 10 (Cycle geodesic on $O(n)$). Since the n -cycle permutation matrix C_n lies in $O(n)$ (and in $SO(n)$ for odd n), the geodesic $I \rightarrow C_n$ on $U(n)$ stays entirely within $O(n)$: the eigenvalues of C_n come in conjugate pairs, so the geodesic matrices are real. All the cycle-geodesic results of Section 4.1 therefore apply equally to $O(n)$. The distinction between orthogonal and

unitary permanents manifests only in the *distributional* behavior, not the geodesic geometry.

6. GAUSSIAN MATRIX ENSEMBLES: HEAVY-TAILED PERMANENTS

The complex Gaussian distribution of $\text{perm}(U)$ for Haar unitaries relies on the CLT heuristic: the permanent is a sum of $n!$ terms, each of magnitude $\sim n^{-n/2}$, and if these are sufficiently decorrelated, a Gaussian limit follows. A natural question is whether this mechanism extends to other natural matrix ensembles. We investigate four Gaussian ensembles:

- **GUE:** $H = (A + A^*)/2$, where A has i.i.d. $\mathcal{CN}(0, 1)$ entries;
- **GOE:** $H = (A + A^T)/2$, where A has i.i.d. $N(0, 1)$ entries;
- **Complex Ginibre:** G with i.i.d. $\mathcal{CN}(0, 1)$ entries;
- **Real Ginibre:** G with i.i.d. $N(0, 1)$ entries.

For each ensemble, we compute 20,000 permanents at each $n \in \{7, 11, 13, 17\}$ using the GPU pipeline.

6.1. Permanents of Hermitian matrices are real.

Proposition 11. *If H is an $n \times n$ Hermitian matrix, then $\text{perm}(H) \in \mathbb{R}$.*

Proof. We have $\overline{h_{ij}} = h_{ji}$, so

$$\overline{\text{perm}(H)} = \sum_{\sigma \in S_n} \prod_{i=1}^n \overline{h_{i,\sigma(i)}} = \sum_{\sigma \in S_n} \prod_{i=1}^n h_{\sigma(i),i} = \sum_{\sigma^{-1} \in S_n} \prod_{j=1}^n h_{j,\sigma^{-1}(j)} = \text{perm}(H),$$

where we used the bijection $\sigma \mapsto \sigma^{-1}$ on S_n . \square

In particular, $\text{perm}(H)$ is real for every GUE matrix, despite H having complex entries. This is confirmed numerically: $|\text{Im perm}(H)|/|\text{Re perm}(H)| < 10^{-14}$ across all 80,000 samples.

6.2. Failure of the CLT: α -stable distributions. The permanent distributions for all four ensembles are spectacularly non-Gaussian: excess kurtosis ranges from 34 (GUE, $n = 7$) to 689 (GOE, $n = 17$) and *increases* with n , opposite to the convergence seen for Haar unitaries. Neither Gaussian nor Student- t distributions provide adequate fits (KS p -values $< 10^{-4}$ for Gaussian; Student- t with fitted degrees of freedom $\nu \approx 1\text{--}2.5$ is better but still rejected).

However, the permanents are well described by α -stable distributions [14]. A symmetric α -stable random variable $X \sim S(\alpha, 0, \gamma, \delta)$ is characterized by its stability index $\alpha \in (0, 2]$: the case $\alpha = 2$ is Gaussian, $\alpha = 1$ is Cauchy, and for $\alpha < 2$ the tails decay as $P(|X| > x) \sim x^{-\alpha}$ (so $\text{Var}[X] = \infty$ for $\alpha < 2$ and $\mathbb{E}[|X|] = \infty$ for $\alpha \leq 1$). We estimate α using both McCulloch's quantile method [13] and regression on the empirical characteristic function; the two methods agree to within ± 0.03 .

Observation 12. *The permanent of an $n \times n$ matrix drawn from each Gaussian ensemble follows a symmetric α -stable distribution with stability index α approximately constant in n :*

	$n = 7$	$n = 11$	$n = 13$	$n = 17$
<i>GOE</i>	1.02	0.99	0.98	0.96
<i>GUE</i>	1.21	1.16	1.18	1.15
<i>Ginibre (real)</i>	1.19	1.17	1.18	1.19
<i>Ginibre (complex)</i>	1.42	1.39	1.39	1.36

In all cases $|\beta| < 0.06$ (symmetric), and KS p-values for the stable fit range from 0.08 to 0.98.

The hierarchy of stability indices is:

$$\alpha_{\text{GOE}} \approx 1.0 < \alpha_{\text{GUE}} \approx \alpha_{\text{Gin-R}} \approx 1.2 < \alpha_{\text{Gin-C}} \approx 1.4 < \alpha_{\text{Haar}} = 2.$$

The GOE permanent is essentially Cauchy-distributed ($\alpha \approx 1$, infinite mean), while the complex Ginibre permanent has the lightest tails among the Gaussian ensembles, yet is still far from Gaussian.

Figure 7 shows the complementary CDF on log-log axes for $n = 13$ (left panel), where the power-law tails are clearly visible and the Gaussian reference drops off too steeply, together with the fitted α as a function of n (right panel), confirming the stability of α across matrix sizes. Figure 8 presents Q–Q plots of the data against fitted stable quantiles for all four ensembles and all four values of n . The agreement along the diagonal confirms the quality of the stable fit across the entire range, including the extreme tails.

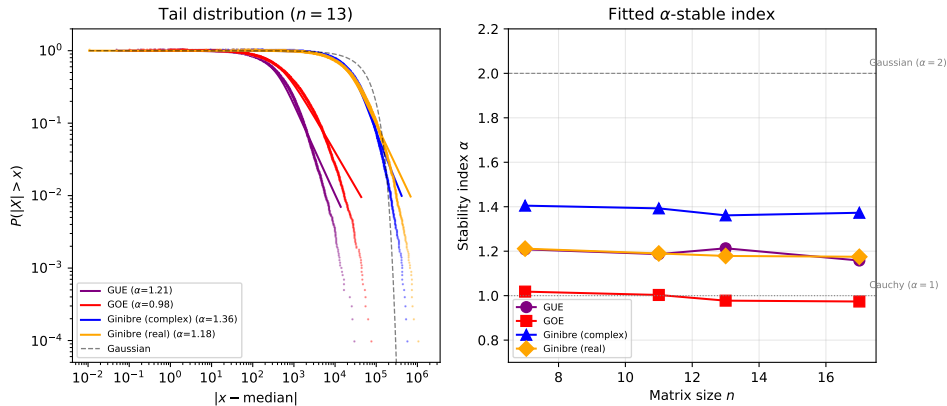


FIGURE 7. Left: complementary CDF (tail distribution) of $|\text{perm} - \text{median}|$ for $n = 13$ across four Gaussian ensembles, with fitted stable distributions (solid curves) and Gaussian reference (dashed). Right: fitted stability index α vs. matrix size n ; $\alpha = 2$ (Gaussian) and $\alpha = 1$ (Cauchy) reference lines are shown.

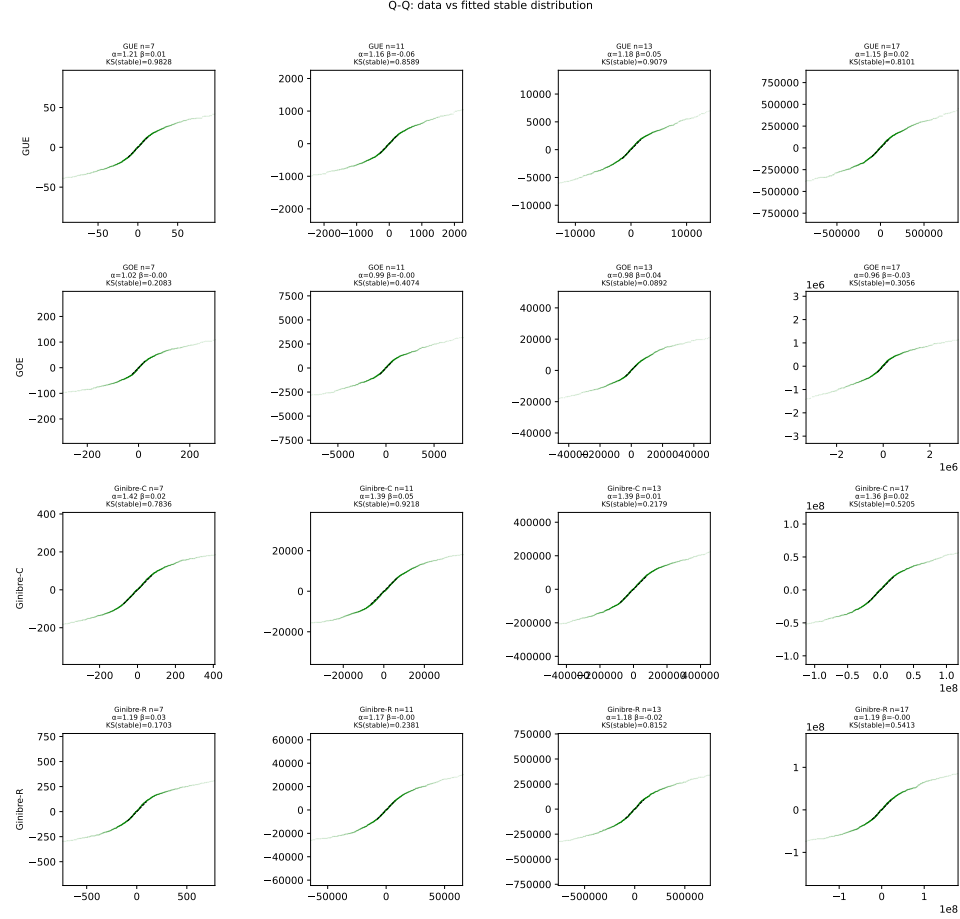


FIGURE 8. Q-Q plots of permanent data (vertical axis) against fitted α -stable quantiles (horizontal axis) for four Gaussian matrix ensembles and $n = 7, 11, 13, 17$ (20,000 samples each). Each panel shows the fitted α , β , and KS p -value. Points falling on the diagonal indicate a good fit.

Remark 13 (Unitarity is essential for Gaussianity). The key difference between Haar unitaries (where $\text{perm}(U)$ is Gaussian) and the Gaussian ensembles (where it is α -stable with $\alpha < 2$) is that unitary matrices have *bounded* entries ($|U_{ij}| \leq 1$), while Gaussian matrices have unbounded entries. When all entries are $O(n^{-1/2})$, the $n!$ terms in the Ryser sum are comparable in magnitude, producing good CLT-like cancellation. For Gaussian matrices, occasional large entries create heavy-tailed products that dominate the sum, destroying the CLT mechanism and producing stable (rather than Gaussian) limits.

7. DISCUSSION

7.1. Relation to prior work. The complex Gaussian observation (Observation 1) complements work on the moments and anti-concentration of unitary permanents. Nezami [10] computed exact moments $\mathbb{E}[|\text{perm}(U)|^{2k}]$ via representation theory and established an asymptotic expansion. The Permanent Anti-Concentration Conjecture (PACC), central to the hardness of boson sampling, asserts that $\Pr[|\text{perm}(U)|^2 \geq n!/\text{poly}(n)] \geq 1/\text{poly}(n)$ for Haar-random U ; recent progress includes [4, 5]. Our complex Gaussian observation identifies the *full distributional form* of $\text{perm}(U)$, not just tail bounds. If proven, it would imply sharp anti-concentration constants. The α -stable distributions for Gaussian ensembles (Section 6) appear to be entirely new and suggest that the Gaussianity of $\text{perm}(U)$ for Haar unitaries is a delicate consequence of the boundedness of unitary matrix entries.

The geodesic results (Observations 4–8) appear to be entirely new. The midpoint formula $\text{perm}(\gamma(\frac{1}{2})) = (-1)^{(n-1)/2} \cdot 2e^{-n}(1 + \frac{1}{3n} + \dots)$ is supported by high-precision numerics and likely admits a proof via saddle-point analysis of the Ryser formula applied to the explicit circulant (2).

7.2. The universal function $f(t)$. The function $f(t) = -\frac{1}{n} \ln |\text{perm}(\gamma(t))|$ for the n -cycle geodesic appears to satisfy:

- $f(t) = f(1-t)$ (from the symmetry $\text{perm}(\gamma(t)) = \overline{\text{perm}(\gamma(1-t))}$);
- $f(t) \sim \frac{\pi^2}{3}t^2$ as $t \rightarrow 0^+$;
- $f(\frac{1}{2}) = 1$ (the $2e^{-n}$ asymptotic).

Finding a closed form for $f(t)$ is an attractive open problem. The initial quadratic $\pi^2 t^2/3$ corresponds to a Gaussian decay $|\text{perm}(\gamma(t))| \approx e^{-n\pi^2 t^2/3}$ near the identity, suggesting a connection to the spectral properties of the skew-Hermitian generator $\log C_n$.

7.3. Connections to boson sampling. Our results bear on several aspects of the boson sampling program [1].

Porter–Thomas statistics. In an n -photon linear optical network described by a Haar-random unitary U , the probability of detecting one photon in each of n specified output modes is $p(T) = |\text{perm}(U_T)|^2/(n_1! \cdots n_m!)$, where U_T is the corresponding $n \times n$ submatrix. For the collision-free case ($n_i \in \{0, 1\}$), this reduces to $p(T) = |\text{perm}(U_T)|^2$. The same CLT heuristic that drives the full permanent toward $\mathcal{CN}(0, \sigma^2)$ applies to submatrix permanents, and the exponential law (1) therefore predicts that the output probabilities follow Porter–Thomas statistics [9]: an exponential distribution with mean $n!/n^n$ (for n -mode submatrices of a Haar-random $n \times n$ unitary). This has been verified experimentally in photonic boson sampling demonstrations [16].

Anti-concentration. The Permanent Anti-Concentration Conjecture (PACC), central to the hardness of approximate boson sampling [1, 4], asserts that

$$\Pr[|\text{perm}(U)|^2 \geq n!/\text{poly}(n)] \geq 1/\text{poly}(n).$$

The exponential form (1) gives the *much* stronger

$$\Pr[|\text{perm}(U)|^2 \geq \sigma^2/\text{poly}(n)] = e^{-1/\text{poly}(n)} = 1 - 1/\text{poly}(n),$$

so *almost all* Haar-random permanents exceed the PACC threshold. Proving the complex Gaussian distributional form would therefore resolve the PACC with room to spare. Even short of a full proof, establishing that $\text{perm}(U)$ is sub-Gaussian (which requires only controlling the moment-generating function) would suffice.

DFT interferometers. The DFT outlier phenomenon (Observation 3) is relevant to experiments using Fourier multi-port interferometers [3], where the large permanent of the DFT matrix suggests that certain transition amplitudes are anomalously large compared to generic unitaries. This complements the suppression laws of Tichy [12], which identify *vanishing* submatrix permanents of the DFT.

Classical simulation frontier. From a computational perspective, the fastest known classical algorithm for exact boson sampling probabilities requires computing the permanent in $O(n 2^n)$ time [2, 11]. Our GPU-accelerated pipeline demonstrates that pushing exact permanent computation to $n \approx 43$ is now feasible, which overlaps with the regime of current photonic experiments [16].

7.4. Open problems.

- (1) Prove that $\text{perm}(U)$ converges in distribution to a circularly-symmetric complex Gaussian (after appropriate scaling) as $n \rightarrow \infty$. For the orthogonal case, determine the rate at which the excess kurtosis of $\text{perm}(O)$ vanishes.
- (2) Prove the midpoint formula $\text{perm}(\gamma(\frac{1}{2})) = (-1)^{(n-1)/2} \cdot 2e^{-n}(1 + \frac{1}{3n} + O(n^{-2}))$.
- (3) Find a closed form for the universal function $f(t)$.
- (4) Explain the prime-vs-composite dichotomy for the DFT geodesic (Observation 8).
- (5) Prove that the permanent of a GOE matrix converges in distribution (after centering) to a Cauchy law, and determine α analytically for the other Gaussian ensembles.
- (6) Extend the table of $\text{perm}(S_n)$ further; $n = 45$ is within reach (~ 28 GPU-hours).

REFERENCES

- [1] S. Aaronson and A. Arkhipov, *The computational complexity of linear optics*, Theory of Computing **9** (2013), 143–252.
- [2] P. Clifford and R. Clifford, *The classical complexity of boson sampling*, Proc. 29th ACM-SIAM Symp. Discrete Algorithms (SODA), 2018, 146–155. arXiv:1706.01260.
- [3] A. Crespi, R. Osellame, R. Ramponi, et al., *Suppression law of quantum states in a 3D photonic fast Fourier transform chip*, Nature Communications **7** (2016), 10469.

- [4] B. Fefferman, S. Ghosh, and W. Zhan, *On the permanent anti-concentration conjecture*, arXiv:2407.19561, 2024.
- [5] M. Kwan, M. Sah, and M. Sawhney, *Anticoncentration of random vectors via the strong perfect graph theorem*, arXiv:2411.04566, 2024.
- [6] D. Scheinerman, *Fast computation of permanents over \mathbb{F}_3 via \mathbb{F}_2 arithmetic*, arXiv:2407.20205, 2024. (Parallelization via Gray code blocks is described in Section 3.1.)
- [7] H. Minc, *Permanents*, Encyclopedia of Mathematics and Its Applications, vol. 6, Addison-Wesley, 1978.
- [8] F. Mezzadri, *How to generate random matrices from the classical compact groups*, Notices AMS **54**(5) (2007), 592–604.
- [9] C. E. Porter and R. G. Thomas, *Fluctuations of nuclear reaction widths*, Physical Review **104** (1956), 483–491.
- [10] S. Nezami, *Permanent of random matrices from representation theory: moments, graphs, and asymptotic expansion*, arXiv:2104.06423, 2021.
- [11] H. J. Ryser, *Combinatorial Mathematics*, Carus Mathematical Monographs 14, MAA, 1963.
- [12] M. C. Tichy, *Sampling of partially distinguishable bosons and the relation to the multidimensional permanent*, Physical Review A **91** (2015), 022316. arXiv:1410.7687.
- [13] J. H. McCulloch, *Simple consistent estimators of stable distribution parameters*, Communications in Statistics—Simulation and Computation **15**(4) (1986), 1109–1136.
- [14] G. Samorodnitsky and M. S. Taqqu, *Stable Non-Gaussian Random Processes*, Chapman & Hall, 1994. See also J. P. Nolan, *Stable Distributions—Models for Heavy Tailed Data*, Birkhäuser, 2020.
- [15] L. G. Valiant, *The complexity of computing the permanent*, Theoretical Computer Science **8** (1979), 189–201.
- [16] H.-S. Zhong, H. Wang, Y.-H. Deng, et al., *Quantum computational advantage using photons*, Science **370** (2020), 1460–1463.

MATHEMATICS DEPARTMENT, TEMPLE UNIVERSITY
Email address: `rivin@temple.edu`